applied sciences

MDPI

Article

Experimental Investigation of the Effect of Delay Time on Rock Fragmentation in Multi-Hole Bench Blasting

Hong-Liang Tang [1], Jun Yang [1,*] and Qi Yu [2]

[1] State Key Laboratory of Explosion Science and Technology, Beijing Institute of Technology, Beijing 100081, China; thlluck@foxmail.com
[2] China Safety Technology Research Academy of Ordnance Industry, Beijing 100053, China; lessno@foxmail.com
* Correspondence: yangj@bit.edu.cn

Abstract: Rock fragmentation by blasting influences ore recovery and the cost of downstream operations. The development of electronic detonators makes it possible to improve fragmentation by controlling the initiation timing in blasting projects, and the effect of the mechanism of delay timing on rock fragmentation should be studied. Fragmentation of granite bench specimens with different initiation timing was investigated in blast experiments. Conclusions are obtained by studying the surface strain field and post-blast specimens. A total of six blasting tests were carried out on granite bench specimens with four boreholes each having a diameter of 10 mm and a length of 450 mm. Each borehole used pentaerythritol tetranitrate (PETN) as the explosive charge, which was approximately 4.84 g with a charge diameter of 5.5 mm. Delay times between adjacent boreholes in the same row were set as 0, 50, 100, 150, 200, and 250 μs. The surface strain field of the bench specimen under blast loading was analyzed using three-dimensional digital image correlation (3D-DIC) techniques based on two cameras that captured high-speed images. Additionally, the post-blast specimen was also observed and recorded. Fragments of each bench specimen were carefully collected, weighed, and sieved with a set of sieves, including very fine particles. According to the 3D-DIC analysis for bench specimens, the propagation pattern of the main strain concentration zone transformed from horizontal to vertical with the increase in inter-hole delay. The maximum blast excavation weight was obtained by the bench specimen with an inter-hole delay of 100 μs, while the bench specimen with the longest inter-hole delay (250 μs) obtained the minimum blast excavation weight. By combining the results for blast excavation weight with the results from fragment size distribution analysis of all specimens, the optimal inter-hole delay was 200 μs. Compared to simultaneous detonation, the median size was decreased by about 14.5% for the inter-hole delay of 200 μs. The results of experiments show that delay time significantly influences rock fragmentation, but the stress wave superposition in short delays cannot improve rock fragmentation. For long delays, the blast-induced crack propagation time should be regarded as an influential factor when choosing the proper delay time. The experimental findings of this study could provide a better understanding of the effect of the mechanism of delay time on rock fragmentation.

Keywords: blast loading; delay time; 3D-DIC analysis; surface strain field; fragment size distribution

check for updates

Citation: Tang, H.-L.; Yang, J.; Yu, Q. Experimental Investigation of the Effect of Delay Time on Rock Fragmentation in Multi-Hole Bench Blasting. *Appl. Sci.* **2023**, *13*, 7329. https://doi.org/10.3390/app13127329

Academic Editor: Ricardo Castedo

Received: 22 May 2023
Revised: 16 June 2023
Accepted: 19 June 2023
Published: 20 June 2023

Copyright: © 2023 by the authors. Licensee MDPI, Basel, Switzerland. This article is an open access article distributed under the terms and conditions of the Creative Commons Attribution (CC BY) license (https://creativecommons.org/licenses/by/4.0/).

1. Introduction

Drilling and blasting technology has been widely used in mining and tunneling as an economical and efficient approach for rock breaking [1,2]. In hard rock mining practice, the immediate release of explosive energy in the blast hole can break the surrounding rock material [3]. However, to date, the results of blasting in projects such as rock excavation have not been satisfactory [4]. The empirical design of blast operation results in low energy efficiency, which may lead to mineral loss, high ground vibration, explosive wastage, and even safety accidents [5–9]. To optimize blasting design and make rock blasting more

efficient, improvement in the understanding of rock fragmentation induced by blast loading is essential.

Research on rock fragmentation mechanisms has been conducted for decades. In the early studies, there were two views on the rock fragmentation mechanism. One view was that rock fragmentation was mainly caused by stress waves [10,11]. Another view was that explosive gas played the dominant role in rock fragmentation [12,13]. Since the 1970s, a more acceptable view of the rock fragmentation mechanism has been found, i.e., the combined effect of stress waves and explosive gas dominates rock fragmentation [14–17]. According to the fracture characteristics around a blast hole under blast loading, the damaged area around the blast hole is usually divided into the borehole expansion zone, crushed zone, fracture zone, and vibration zone from near to far [6,18,19]. After the explosive column in the blast hole is detonated, radial and circumferential cracks are generated around the blast hole under the influence of the stress wave and gas pressure [20]. When the stress wave propagates to the free surface, the reflected tensile wave will induce the fracturing of the surface rock. Holloway [21] studied crack propagation using granite specimens. The study showed that radial cracks initiated from the surface and propagated inward, that spalling cracks formed near the free surface, and that other radial cracks propagated from the blast hole. As the cracks develop and intersect within the rock, the rock is broken into fragments that can be moved under the effect of expanding gases [22].

For a long time, optimizing blasting design to obtain better fragmentation has been a hot study topic for researchers and engineers. The emergence of electronic detonators has allowed for more precise control of detonation time, which has led to more attention being given to study of the effect of delayed initiation on rock damage and fragmentation, especially the influence of stress wave interaction on fragmentation. Rossmanith [23,24] used Lagrange diagrams to analyze the stress wave superposition in two adjacent boreholes with different detonation times. He concluded that stress wave superposition positively affects rock fragmentation and that using a short delay time between two boreholes is beneficial in achieving uniform rock fragmentation. Influenced by the study of Rossmanith, Vanbrabant and Espinosa [25] performed field tests using short delays between blast holes. Their field test results indicated a dramatic improvement in rock fragmentation using short delay times compared to long delay times, with a 45.6% improvement in median size. Chiappetta [26] concluded, according to image analysis of blast fragments and statistics of fragment sizes, that the delay time needs to be sufficiently short to allow for the interaction of stress waves between adjacent boreholes.

However, as more relevant studies were conducted, the view that the stress wave superposition is not the dominant factor in improving rock fragmentation appeared. Johansson and Ouchterlony [27] conducted blasting tests using concrete bench specimens to investigate the influence of stress wave interactions on fragmentation. Their study showed there is not enough experimental evidence suggesting that short delays with shock wave interactions can obtain better fragmentation than long delays. Katsabanis et al. [28] performed small-scale blasting tests on granite bench specimens, and the experimental results showed that the worst result was obtained by simultaneous detonation. They found that fragmentation improved with increased delay time, with fragment size stabilizing when delay time was longer than 11 ms/m of burden. Stagg and Rholl [29] investigated the effect of timing on fragmentation. Their results indicated that the best fragmentation could be obtained by detonating the second blast hole when the damage process of the first blast hole reached its final state. Tang et al. [30] used double-hole bench specimens to study the influence of delay time on rock fragmentation. Their study indicated that a long delay without stress wave superposition obtained the best blasting excavation quality. Schill and Sjöberg [31] investigated the effect of accurate detonation on rock fragmentation through the use of a 3D model in LS-DYNA. In their numerical study, the influence of stress wave interaction on fragmentation was limited and occurred in localized zones. In the theoretical and numerical studies of Yi et al. [32,33], they indicated that when the stress waves between two blast holes are superposed, tensile stress increases in a small region

around the interaction point, which cannot improve fragmentation. Blair [34] questioned the positive influence of stress wave superposition on fragmentation, stating that stress wave interactions were uncertain in the 3D model and that stress wave superposition had a limited effect on fragmentation.

In mining and tunneling, the purpose of optimizing rock blasting projects is to obtain better rock fragmentation. Compared to poor fragmentation, uniform rock fragmentation can improve ore recovery and reduce the energy consumption of crushing and grinding processes in the practice of mining operations. As rock fragmentation by blasting influences a realistic mine-to-mill process, fragment size distribution is an important issue to study. Zhang et al. [35] investigated rock fragmentation under different constraint conditions by analyzing fragment size distribution. Chi et al. [36] performed blast experiments using cylinder specimens with different decoupling ratios. The analysis of fragment size distribution showed that the decoupling ratios and the filling materials in the blast hole have a significant influence on rock fragmentation. Cho et al. [37] conducted two bench blasting experiments in the field and estimated fragment sizes using sieving data and image analysis. Furthermore, they proposed a numerical simulation method to predict the fragment size distribution. In the 12 full-scale bench blast tests performed by Sanchidrián et al. [38], the fragmentation results were compared using the fitted curve of fragment size distribution. In addition, they used the fragmentation–energy fan concept to establish a relationship between the fragment size distribution and the explosive energy concentration. Hashemi and Katsabanis [20] investigated rock fragmentation in multi-hole blasting through the use of LS-DYNA numerical code. In their study, the influence of stress wave interaction on fragmentation was investigated by fragment size distribution analyzed from WipFrag.

The objective of this paper is to study the effect of delay time on rock fragmentation in multi-hole bench blasting. Six small-scale blast tests were conducted with the purpose of providing experimental data. In Section 2, the material properties of the granite, the dimensions of the bench specimen, the devices of the experiment, and the combination measurement system of the high-speed cameras and the 3D-DIC are illustrated. In Section 3, the surface strain fields of three bench specimens with different delay times are compared and analyzed. The post-blast pattern and blast excavation weight of specimens with different delay times are compared. Furthermore, the extended Swebrec function is employed to fit the curves of the fragment size distribution for all specimens. In Section 4, the stress wave propagation of the first three tests is briefly analyzed in the two-dimensional (2D) horizontal plane. According to the experimental results, the factors other than stress waves affecting blasting excavation quality are discussed. Finally, Section 5 presents the conclusions of this study.

2. Experiment

2.1. Granite Material

Bench specimens of granite from the Zhangqiu District (Jinan, China) were utilized in this study. The material properties of the Zhangqiu granite were measured by static tests according to a TBM machine (Sunstest, Guangzhou, China) with a loading rate of 0.1 $kN \cdot s^{-1}$. The uniaxial static compressive strength test was performed on cylindrical specimens with a diameter of 50 mm and a length of 100 mm. Splitting tests were carried out on disc specimens 50 mm in diameter and 20 mm in thickness to determine static tensile strength. Additionally, the longitudinal wave (P-wave) velocity of the granite rock was tested. Five replicate tests were performed for each rock property, from which the average value was determined. The material properties of the Zhangqiu granite are shown in Table 1.

Table 1. The material properties of Zhangqiu granite.

Density (g cm^{-3})	Young's Modulus (GPa)	Poisson's Ratio	Uniaxial Static Compressive Strength (MPa)	Static Tensile Strength (MPa)	Longitudinal Wave Velocity (m s^{-1})
2.61	13.69	0.21	69.08	5.65	3383

For the Zhangqiu granite used in this paper, quartz (63 wt%) and feldspar (21 wt%) with grain sizes ranging from 1.2 to 10.2 mm were the principal visible minerals. The main heavy mineral of Zhangqiu granite is magnetite (0.29 wt%), with a particle size range of 0.04 to 0.25 mm. The other heavy minerals are primarily in the particle size range of 0.03 to 0.45 mm. Figure 1 shows a thin-section image of Zhangqiu granite.

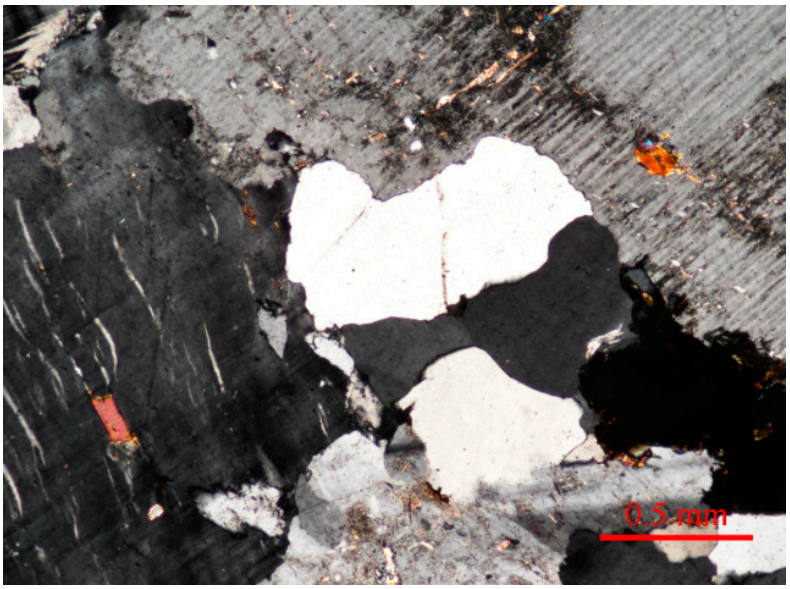

Figure 1. Thin-section image of Zhangqiu granite.

2.2. Specimen and Explosive

One delivery of uniform granite was utilized to make the bench specimens. The basic dimensions of the bench specimens with four vertically drilled through-holes were 679 mm × 548 mm × 450 mm. The through-holes 16 mm in diameter were drilled in two rows, each with two through-holes. There was 120 mm between adjacent through-holes in the same row, and the distance between the adjacent rows was 104 mm. Figure 2 shows the dimensions of the bench specimen. The surface of the bench specimen had no visible pre-existing cracks.

The granular pentaerythritol tetranitrate (PETN) was packed into a plastic tube 5.5 mm in diameter and 240 mm in length, with a charge weight of about 4.84 g and a charge density of approximately 0.85 g/m^3 for each borehole. Each end of the tube was wrapped with black tape to form a lining equal to the diameter of the borehole to make sure the explosive column was positioned at the center of the borehole. In order to provide accurate delayed initiation between boreholes, the initiation timing of the explosive columns in the boreholes was controlled by changing the length of detonating cord, referring to the detonation method used in previous studies [27,30]. According to the information from the supplier, the detonating cord had a linear density of 4.25 g/m and a detonation velocity of 6850 m/s. A steel tube with a length of 60 mm was used at the bottom of the borehole to separate the detonating cord from the wall of the borehole to reduce the impact of the detonating cord on the bench specimen. Figure 3 shows a set of assembled explosive

devices. The experimental number, inter-hole delay, and charge weights of each bench specimen are presented in Table 2. In each blast experiment, the delay between rows was set as two times the delay time between boreholes.

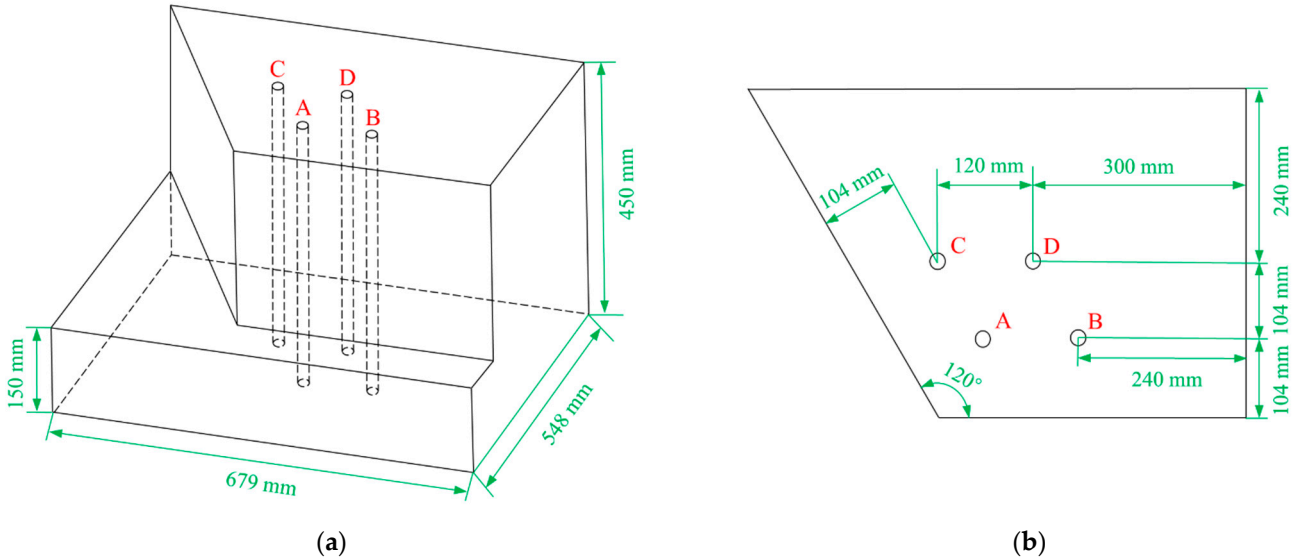

(**a**) (**b**)

Figure 2. Schematic diagram of the bench specimen: (**a**) 3D view of the bench specimen; (**b**) borehole locations on the top surface. The letters A–D represent the numbers of the boreholes.

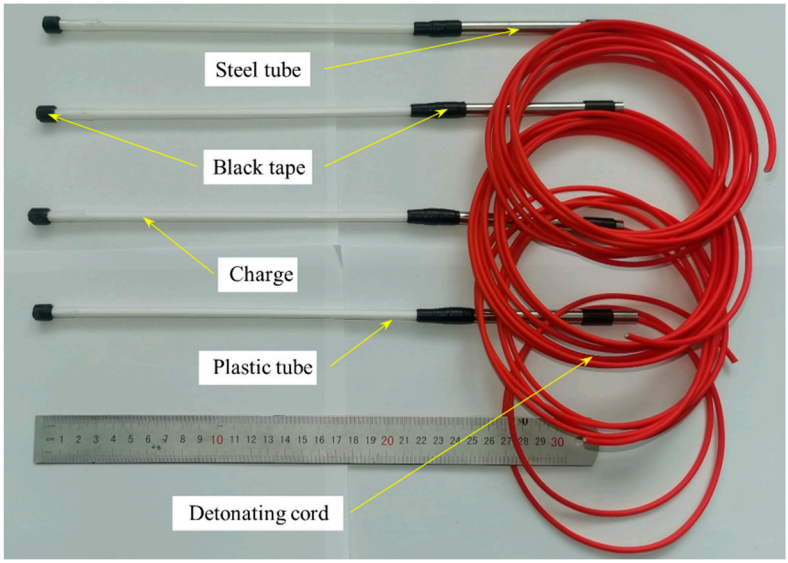

Figure 3. The assembled explosive devices.

Table 2. Inter-hole delays and explosive column weights for all bench specimens.

Bench Specimen No.	Inter-Hole Delay (μs)	Charge Weight of A (g)	Charge Weight of B (g)	Charge Weight of C (g)	Charge Weight of D (g)
BS1	0	4.83	4.84	4.82	4.85
BS2	50	4.84	4.85	4.86	4.86
BS3	100	4.86	4.83	4.85	4.84
BS4	150	4.85	4.83	4.84	4.86
BS5	200	4.83	4.85	4.86	4.84
BS6	250	4.84	4.86	4.83	4.84

2.3. Experiment Setup

To reduce the diameter of the vertical through-holes, steel rods 10 mm in diameter and 550 mm in length were positioned at the center of each vertical through-hole before the blasting experiments were carried out. Cement mortar was used as a filling medium and was filled into the gap between the steel rod and the wall of the borehole. After the cement mortar was solidified and had a certain strength, the steel rods were removed. When the diameter of the borehole was reduced to 10 mm, given the diameter of the explosive column, the decoupling ratio was 1.8 for all bench specimens. In the blasting test, the top of the explosive column inserted in the borehole was 100 mm down from the top of the bench specimen, and cement mortar was selected as the stemming to be filled into the borehole. Figure 4 shows a cross-sectional view of the first row with the explosive devices assembled in the boreholes.

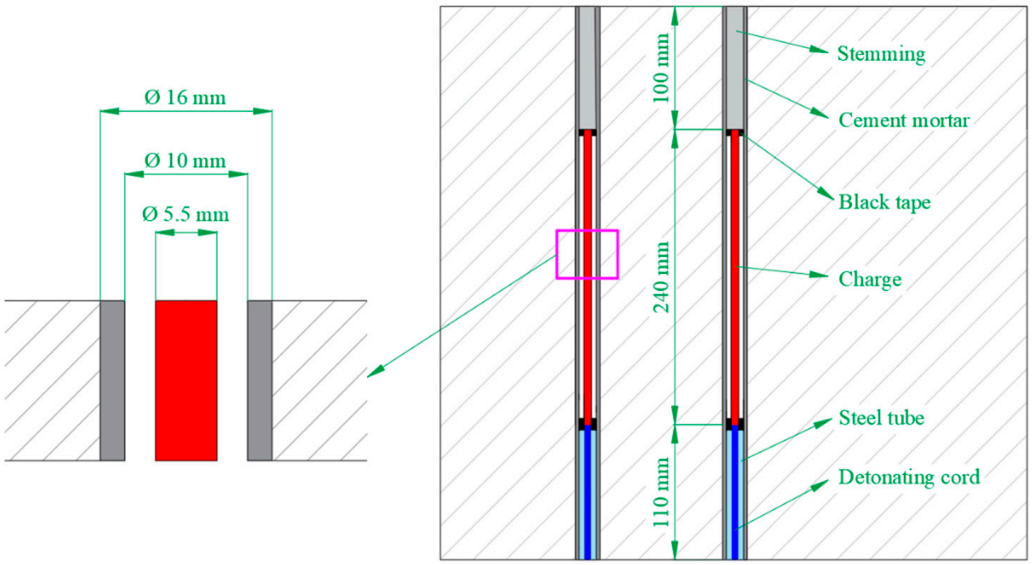

Figure 4. Cross-section of the first row with the explosive devices assembled in the boreholes.

Before the experiment, the bench specimen was assembled in a constraint device. The constraint device consisted of three steel plates, six steel sticks, and some bolts. Three steel plates with a thickness of 20 mm were welded together, and steel sticks were located on the left and front sides of the bench specimen and bolted to the bottom steel plate. The purpose of manufacturing the constraint device was to make the boundary conditions of the bench specimen match the bench in the field. The assembled bench specimen and constraint device are shown in Figure 5.

The blast experiments were carried out in an explosion chamber at the Beijing Institute of Technology. Figure 6 illustrates a schematic diagram of the blasting experiment. The detonating cords in each experiment were detonated by an electric detonator. While the detonator was detonated by a direct current, the trigger signal would simultaneously start two high-speed cameras to monitor the fracturing process of the bench specimen under blast loading.

The fragments produced by the bench specimen in the explosion chamber were carefully collected, and the post-blast bench specimen was observed and recorded after each blasting test. Furthermore, the collected fragments were weighed and sieved. The obtained sieving data would be fitted to analyze and compare fragment size distribution.

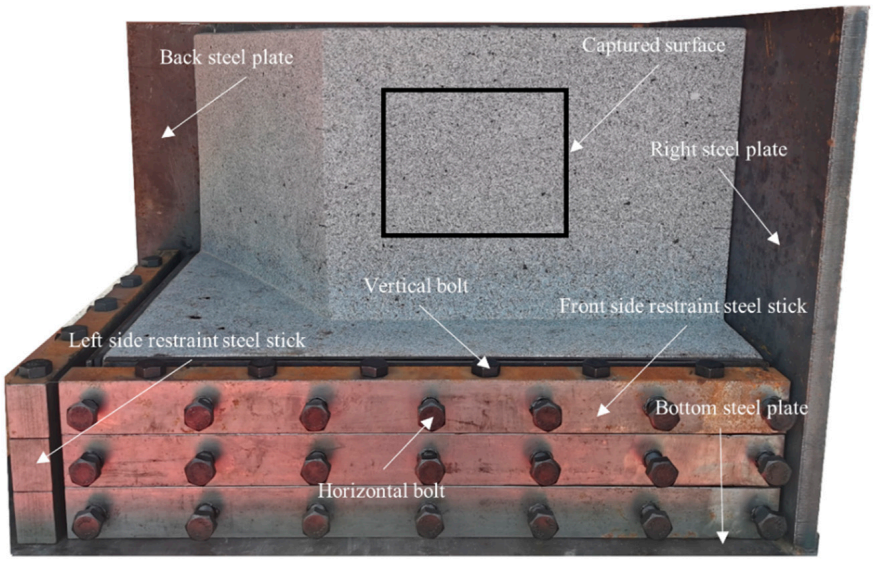

Figure 5. The assembled bench specimen and constraint device.

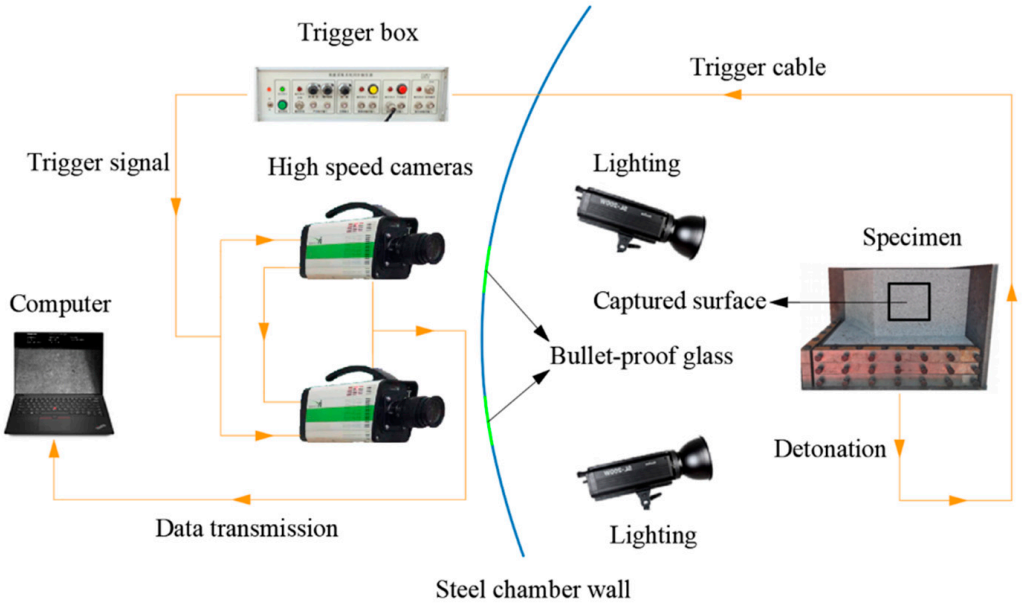

Figure 6. Schematic diagram of the blasting experiment.

2.4. High-Speed Cameras and DIC

In each blasting test, two high-speed cameras (i-SPEED 716, IX-Cameras Inc., Rochford, Essex, UK) were used to monitor the breakage process of the bench specimen. The two high-speed cameras were placed outside the explosion chamber and captured the process through two inspection windows. The area of interest (AOI) on the front surface of the specimen is shown in Figure 7. The square drawn in purple was the field of the AOI, which was approximately 180 × 160 mm^2. Two different settings of high-speed cameras were utilized in the blasting tests. Specifically, 20,000 frames per second (fps) and an image resolution of 1064 × 762 pixels was used in BS1 and BS2. In BS3–BS6, 30,000 fps and an image resolution of 840 × 624 pixels was used.

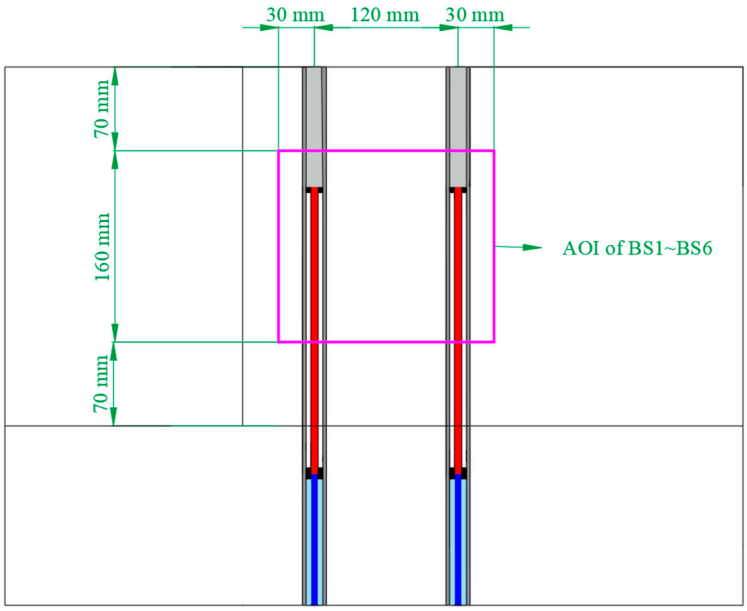

Figure 7. The location of the AOI on the front surface of the bench specimen.

DIC can analyze high-speed images to obtain field shape, deformation, or motion measurements [39]. With the development of the non-contact full-field measurement method, its use in rock testing has been widely adopted. Lenoir [40], Bornert [41], and Hedan [42] used the DIC technique to test rock surface strain under quasi-static loading. Cheng et al. [43] applied the 3D-DIC technique in uniaxial compression tests of composite rock specimens to investigate the development of the strain field. In rock tests under dynamic loading, Xing et al. [44] investigated the full-field strain and strain rate fields of rock materials using the 3D-DIC technique. To investigate the morphological characteristics of dynamic tensile fractures in brittle materials, Xu et al. [45,46] used the 2D-DIC technique to analyze the full-field tensile strain distribution on the surface of the rock and concrete specimens in the split Hopkinson pressure bar system. Chi et al. [47] studied the dynamic breakage process of granite blocks under blast loading and determined the beginning time of the crack on the surface by strain gauge and DIC analysis. For the full-field strain analysis of the rock surface in this study, commercial 3D-DIC software of version 2018 (MatchID 3D, MatchID NV, Ghent, Belgium) was employed. Corrections were performed using a polymethyl methacrylate (PMMA) calibration plate with a 9 × 10 grid and a spacing of 9 mm. For the processing parameters of 3D-DIC in this study, 23 × 23 pixels and 3 pixels were selected as subset size and step size, respectively.

3. Results

3.1. Full-Field Strain

Dynamic deformation of the rock material under blast loading can be obtained using the 3D-DIC technique and analysis of high-speed images. Full-field strains of the AOI for three specimens (BS1, BS3, and BS5) were obtained. The surface strain field of the AOI was calculated using von Mises strain.

For BS1, the inter-hole delay was 0 μs, i.e., simultaneous detonation. The frame rates of the high-speed cameras were set to 20,000 fps, and the image resolution was set to 1064 × 762 pixels in the experiment. The obtained surface strain fields of eight frames (from 0 to 500 μs) for BS1 are shown in Figure 8, which shows the developing strain pattern. As seen in Figure 8, strain concentrations first occurred in the lower part of the AOI at 200 μs. In the color plots from 250 to 300 μs, there were two clearly horizontal strain concentration zones in the middle and lower part of the AOI. In addition, a vertical strain concentration zone on the lower right side of the AOI intersects with the two horizontal strain concentration zones. At 300 μs, two vertical strain concentration zones formed in the

upper part of the AOI. From 350 to 500 μs, the strain concentration zones became wider and formed macroscopic cracks as time increased. The cracks developed and intersected, breaking the rock into different fragments. From the strain fields analyzed by 3D-DIC, the surface strain development pattern and potential failure zone can be easily estimated.

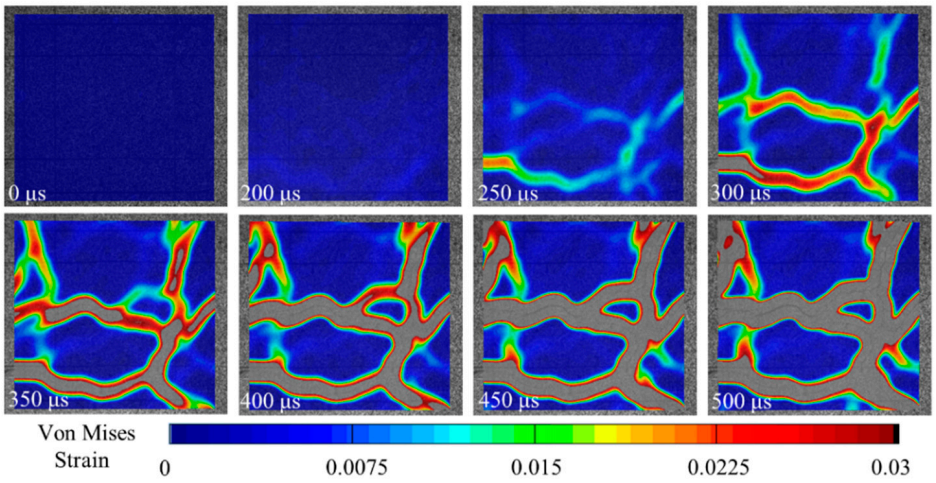

Figure 8. Full-field strain of BS1.

The resolution and frame rate of the high-speed cameras for BS3 was set to 840 × 624 pixels and 30,000 fps, respectively. There was approximately 33.3 μs between adjacent frames. The full-field strain of BS3 is shown in Figure 9, which presents the calculated results obtained by 3D-DIC software from 0 to 566 μs. At 233 μs after the detonation of the detonator, strain concentration was observed on the left side of the AOI. From 266 to 333 μs, the strain concentration zone in the AOI developed upward along the vertical direction. There were secondary strain concentrations near the vertical strain concentration zone at 366 μs. As the effect of blast loading continued, strain concentration zones developed along the horizontal direction formed in the middle and bottom of the surface strain field. It should be noted that strain concentrations were found on the right side of the AOI at 433 μs, though these did not form significant strain concentration zones as time increased. At 566 μs, the middle horizontal strain concentration zone reached the right edge of the surface strain field. Compared with the strain evolution process of BS1, the formation time of the horizontal strain concentration zone for BS3 was relatively late.

BS5, with an inter-hole delay of 200 μs, was selected with the same image resolution and frame rate setting as BS3. Figure 10 shows the surface strain fields for BS5 from 0 to 566 μs. It can be seen that the strain concentration zone of BS5 from 233 to 333 μs mainly appeared on the left side of the AOI, which was similar to that of BS3. From 266 to 366 μs, the left vertical strain concentration zone extended in the middle and branched horizontally. Strain concentration then occurred at 400 μs in the middle of the AOI and formed a horizontal strain concentration zone as time increased. From 500 to 566 μs, a downward developing vertical strain concentration zone appeared in the upper right of the AOI. As time increased, the vertical strain concentration zone intersected with the middle horizontal strain concentration zone.

Figures 8–10 show the evolution of the strain field on the bench specimens with different delay times. The strain fields obtained by the 3D-DIC technique are favorable for observing the dynamic deformation of the specimen surface before the appearance of macroscopic cracks. By comparing the developing strain patterns shown in Figures 8–10, it indicates that the strain field of simultaneous detonation was first observed as the strain concentration zone developed horizontally. However, the strain concentration zone that developed vertically appeared relatively later and developed in a smaller range. As the delay time increased, the vertical strain concentration zone on the surface was fully developed, with the left vertical strain concentration zone mainly developing in both BS3

and BS5 from 0 to 333 μs. This observation indicates that the development pattern of the main strain concentration zone changed from horizontal to vertical as the inter-hole delay increased.

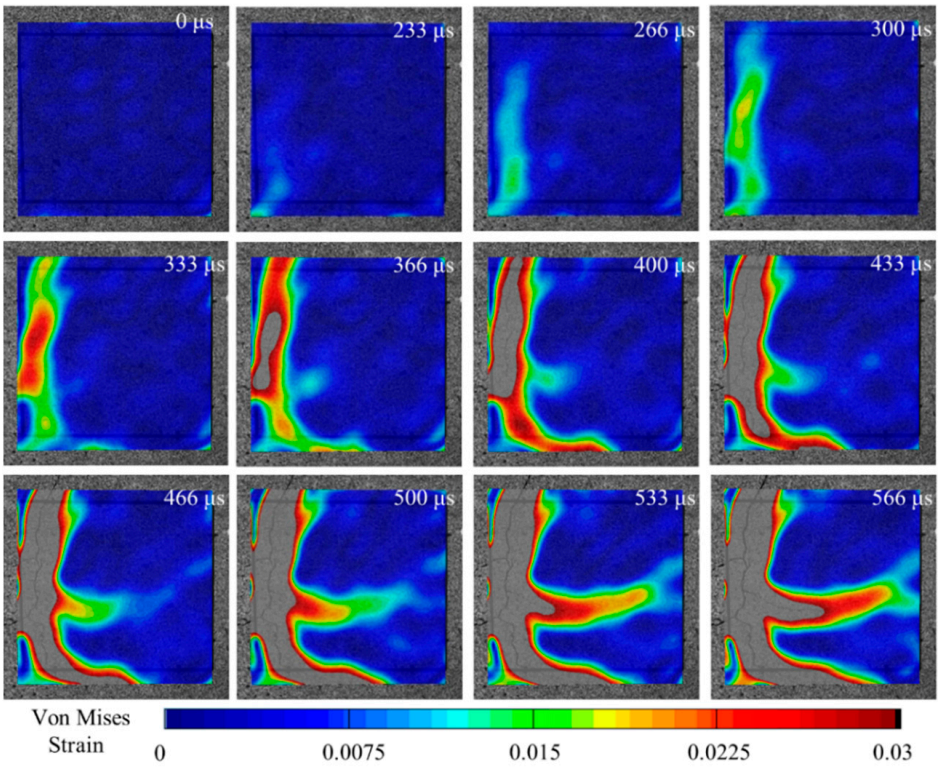

Figure 9. Full-field strain of BS3.

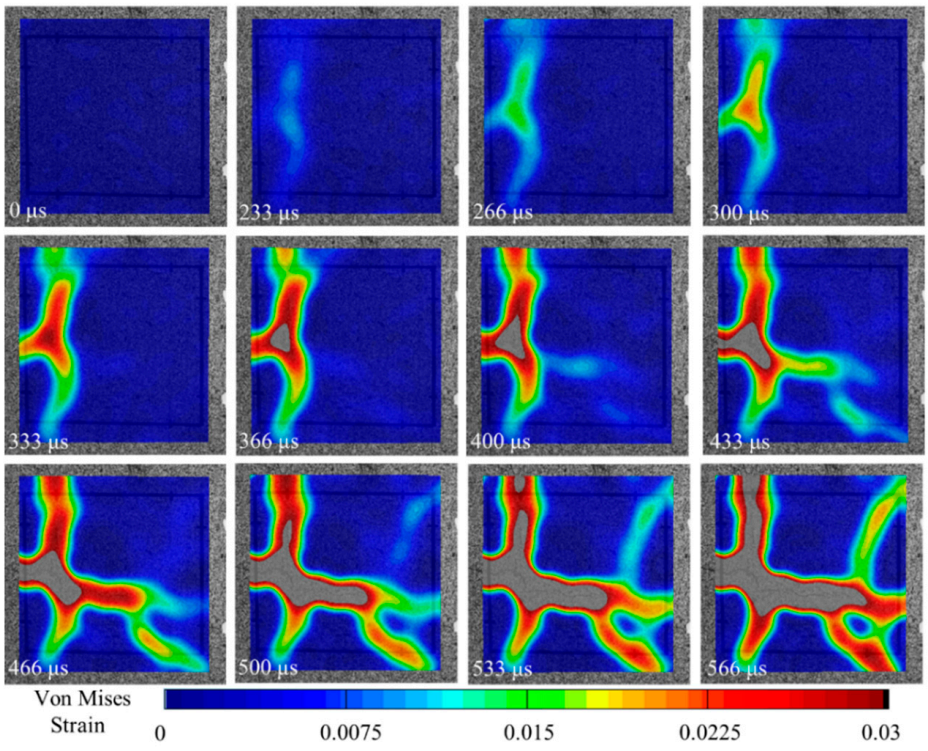

Figure 10. Full-field strain of BS5.

3.2. Blast Excavation Pattern and Weight

The excavation pattern of each bench specimen after blasting is shown in Figure 11. As seen in Figure 11, all bench specimens were severely damaged.

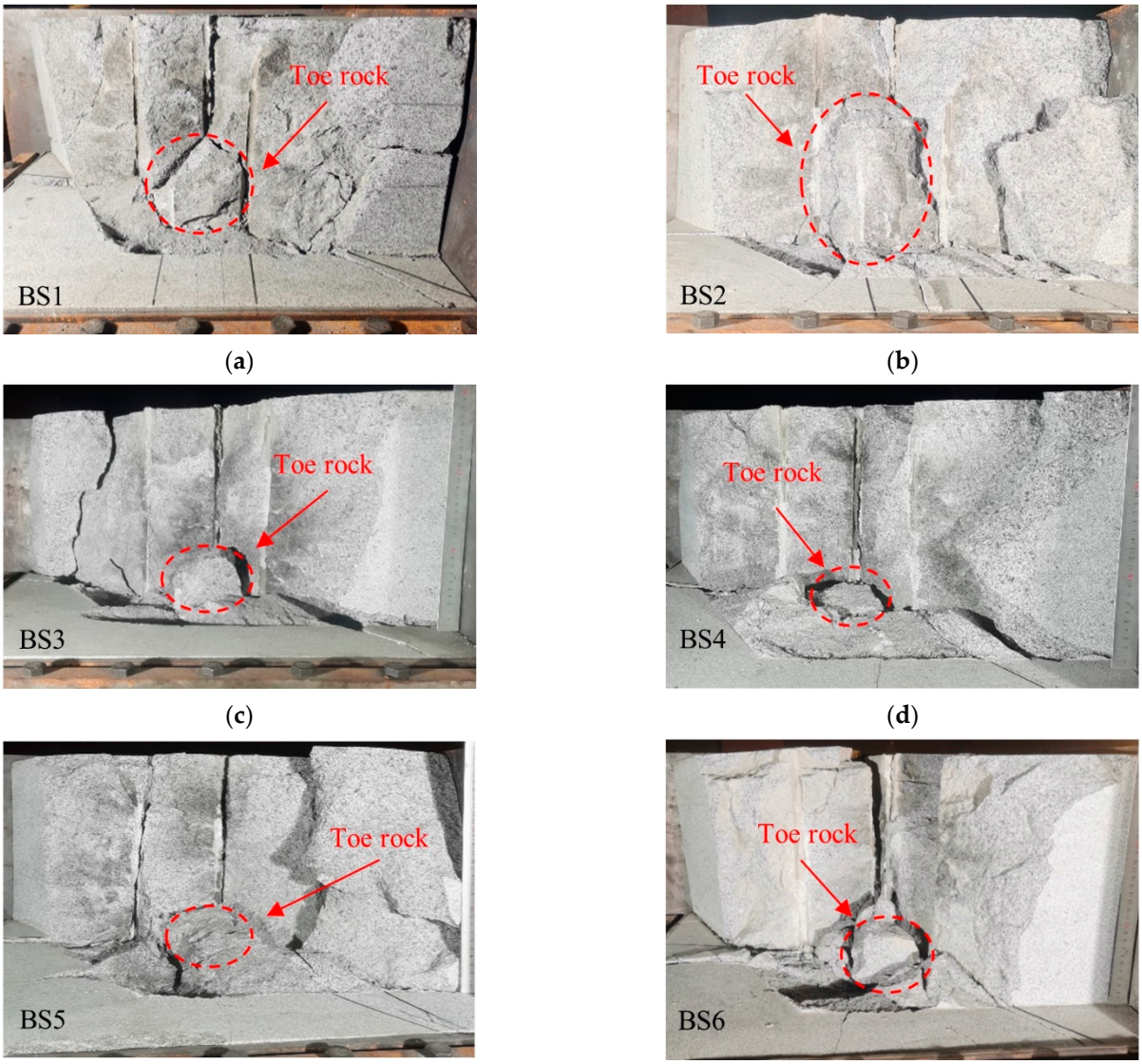

Figure 11. Post-blast pattern of bench specimens: (**a**) post-blast pattern of BS1; (**b**) post-blast pattern of BS2; (**c**) post-blast pattern of BS3; (**d**) post-blast pattern of BS4; (**e**) post-blast pattern of BS5; (**f**) post-blast pattern of BS6.

In the post-blast specimens of BS1–BS3 (0–100 μs), there were toes of rock formed in the area between boreholes above the bench floor. Although the superposition and interaction of stress waves occurred with short delays, the rock mass between boreholes was not sufficiently broken in BS1 and BS2, resulting in the significant generation of toe rock above the bench floor. In the first three experiments, BS2 (50 μs) produced the largest toe rock. With a further increase in delay time, the range of toe rock remaining above the bench floor for BS4 (150 μs) and BS5 (200 μs) decreased. The range of toe rock on the bottom floor of BS6, which had the longest delay (250 μs), presented an increase; however, it was still smaller than that of BS1 and BS2. The post-blast bench specimens indicate that delayed initiation influences the range of toe rock, and the use of a long delay can reduce the amount of toe rock between boreholes compared to a short delay.

To better compare blast excavation results, the blast fragments produced by each bench specimen were weighed. The blast excavation weights of all bench specimens are shown in Figure 12.

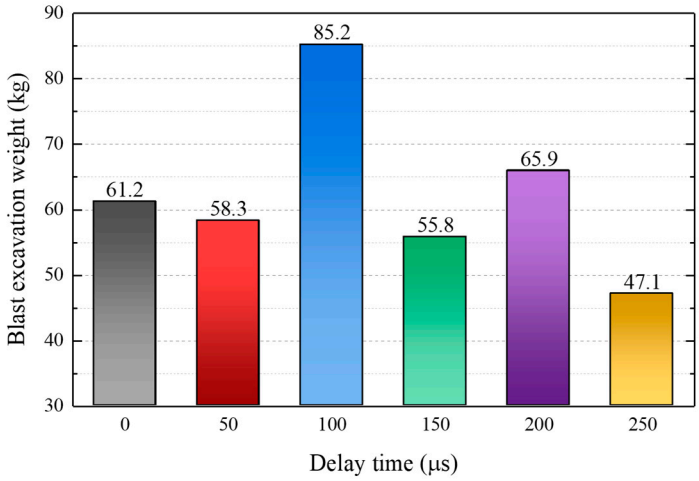

Figure 12. Blast excavation weights of all bench specimens.

As shown in Figure 12, BS1 and BS2 obtained similar fragments weights of 61.2 kg and 58.3 kg, respectively. When the inter-hole delay was increased to 100 μs, the blast excavation weight of BS3 increased to 85.2 kg, which is 1.4 times the weight of blast excavation for simultaneous detonation. However, a further increase in delay time did not continue to increase the blast excavation weight, which was 55.8 kg for BS4 (inter-hole delay of 150 μs). BS5 recorded the second heaviest blast excavation weight of all bench specimens, reaching 65.9 kg. BS6, with the longest inter-hole delay, obtained the minimum blast excavation weight of 47.1 kg. Although the specimen dimensions and the charge weights were the same, there were differences in blast excavation weight at different inter-hole delays, indicating that delay time influences blast excavation weight.

3.3. Fragment Size Distribution

To further study the effect of delay timing on rock fragmentation, the fragments of each bench specimen were screened through a set of 16 standard sieves. The mesh sizes of the standard sieves ranged from 0.048 to 35 mm. The coarse fragments with particle sizes larger than 35 mm were weighed individually. The connected scatterplots of the fragment size distribution for all bench specimens are shown in Figure 13.

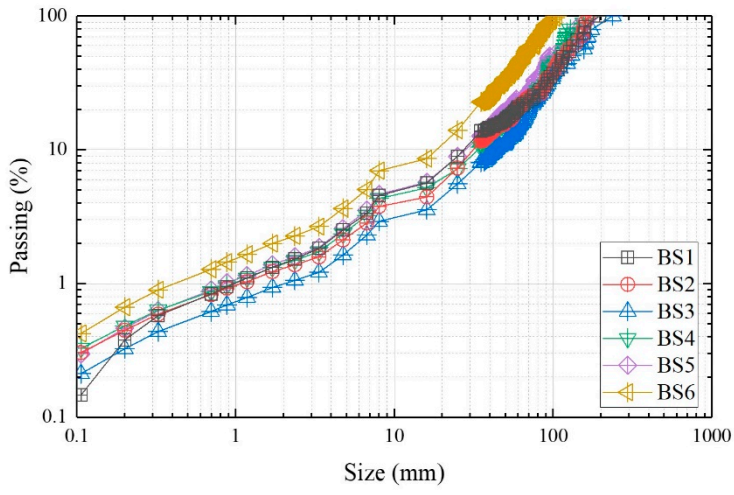

Figure 13. Fragment size distribution for all bench specimens.

Due to the wide size range of fragments, the size distributions of measured data were constructed using the extended Swebrec function, which is considered one of the best-fitting distribution functions to describe rock fragmentation data [48–50]. The extended Swebrec function is a five-parameter distribution whose cumulative distribution, $P(x)$, is as follows [50]:

$$P(x) = \frac{1}{1 + a \cdot \left[\ln(x_{max}/x)/\ln(x_{max}/x_{50})\right]^b + (1-a) \cdot \left[\left(\frac{x_{max}}{x} - 1\right)/\left(\frac{x_{max}}{x_{50}} - 1\right)\right]^c} \quad (1)$$

The five fitting parameters include the maximum size x_{max}, the median size x_{50}, the partition coefficient a, the shape parameter b, and the shape parameter c. Given the wide variation in fragment sizes and accumulated mass passing values, as well as the tendency of an ordinary least squares scheme to match the coarse zone and ignore the fine zone, a weighted least squares scheme was used to fit the curves. In this study, the curves fitted by the extended Swebrec function were made with $1/P^2$ weighting to make the fitted curves more accurate. The corresponding parameters of fitted curves are shown in Table 3.

Table 3. Parameters and goodness of the constructed fitted curves.

Bench Specimen No.	Inter-Hole Delay (μs)	x_{max} (mm)	x_{50} (mm)	a	b	c	R^2
BS1	0	195.4	122.1	0.4604	1.708	0.8526	0.9924
BS2	50	166.3	121.3	0.1085	2.309	0.6165	0.9961
BS3	100	237.1	128.4	0.8099	2.265	0.8727	0.9956
BS4	150	167.4	112.7	0.4377	1.904	07194	0.9945
BS5	200	171.5	103.7	0.4092	2.116	0.7438	0.9969
BS6	250	105.7	65.9	0.4626	1.929	0.7543	0.9981

Figure 14 shows the sieving data for the fragments and the constructed sieving curves. The accumulated mass passing is generally divided into four zones, including mass passing less than 2% (very fine zone), mass passing from 2 to 20% (fine zone), mass passing from 20 to 80% (central zone), and mass passing more than 80% (coarse zone) [51]. A larger particle size represents a coarser fragment at the same mass passing. In the range of the four zones, mass passings of 1%, 10%, 50%, and 100% were selected as the parameters for comparison and analysis. The particle sizes of each bench specimen at the selected four percentages are given in Table 4.

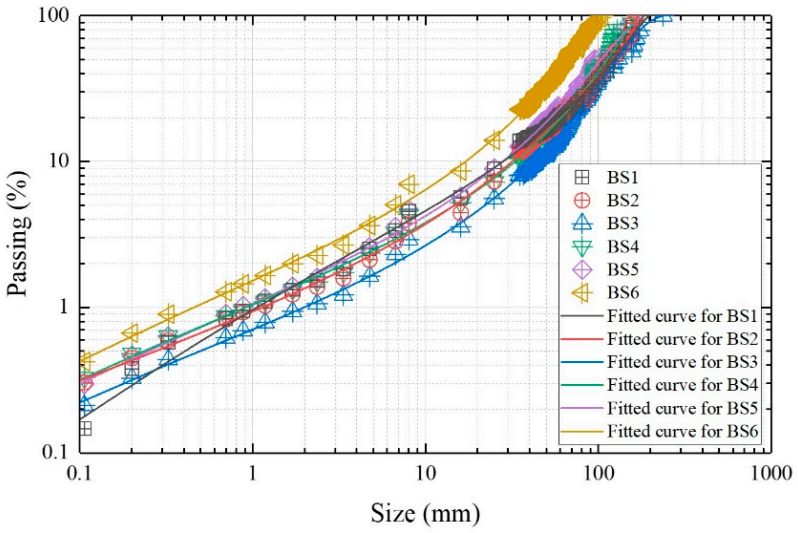

Figure 14. Fitted curves constructed by the extended Swebrec function.

Table 4. The particle sizes at the given four mass passings.

Bench Specimen No.	Inter-Hole Delay (μs)	x_1 (mm)	x_{10} (mm)	x_{50} (mm)	x_{100} (mm)
BS1	0	1.06	28.08	122.1	195.4
BS2	50	1.14	31.72	121.3	166.3
BS3	100	1.99	43.18	128.4	237.1
BS4	150	0.92	33.12	112.7	167.4
BS5	200	0.89	27.69	103.7	171.5
BS6	250	0.46	17.05	65.9	105.7

The fitted curves of the first three experiments are shown in Figure 15. By combining Table 3 and Figure 15, the fitted curves move downward in the range of 1–20% mass passing, indicating that the particle sizes become larger with increasing delay time in this range. However, the fitted curve of BS2 is located above the fitted curve of BS1 in the range of 20–100% mass passing, which indicates that the fragmentation of BS2 was better than that of BS1 in this range. Additionally, the difference in particle size between BS1 and BS2 becomes significant in the coarse zone. Taking 100% passing as an example, the x_{100} of BS1 was 195.4 mm, while the x_{100} of BS2 was 166.3 mm, with the difference between the x_{100} values reaching 29.1 mm. When the inter-hole delay was increased to 100 μs, the particle size produced by BS3 was larger than BS2 in the range of 1–100% passing, which indicated that further increases in inter-hole delay in the range of 50–100 μs were not effectively improved rock fragmentation. The maximum particle size of BS3 reached 237.1 mm, which is 1.4 times larger than that of BS2. The variation in the fragmentation of BS1–BS3 shows that when the inter-hole delay was in the range of 0–100 μs, the delays had less effect on the particle size at 1–50% mass passing. For example, the median sizes of BS1, BS2, and BS3 were 122.1 mm, 121.3 mm, and 128.4 mm, respectively, with insignificant differences. In the blasting experiments of BS1–BS3, the effect of delay time on fragmentation was mainly observed in 50–100% mass passing, especially in the coarse zone.

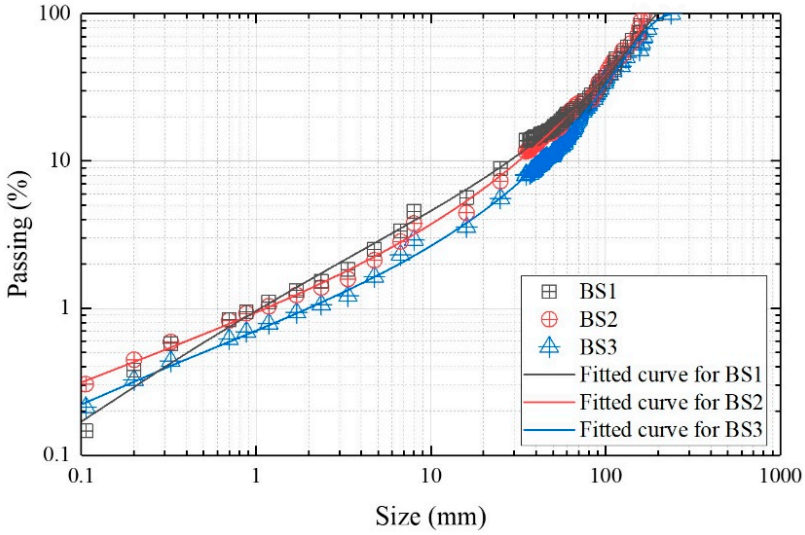

Figure 15. Fitted curves of BS1–BS3.

Figure 16 shows the fitted curves for BS4–BS6 with inter-hole delays in the range of 150–250 μs. In 1–80% mass passing, the fitted curves for the three specimens move upward in log-log space. The movement trend of the fitted curves shows that rock fragmentation improved with the increased inter-hole delay (from 150 to 250 μs). As seen in Figure 16, the fitted curve of BS4 was close to that of BS5, i.e., the difference between the particle sizes at the same mass passing was insignificant. For example, particle size at 10% mass

passing was 33.1 mm and 27.7 mm for BS4 and BS5, respectively, with a difference of 5.4 mm. The particle size of BS6, with an inter-hole delay of 250 μs, was significantly smaller than that of BS4 and BS5 in the mass passing of 1–100%, indicating that fragmentation was significantly improved at this delay time. Compared to BS5, BS6 had decreased values for x_{50} (by about 36.5%) and x_{100} (by about 38.4%). In summary, BS6 produced the most uniform rock fragmentation.

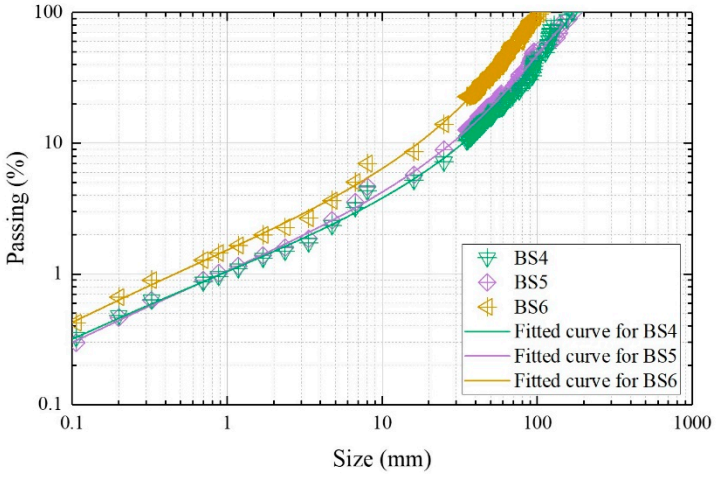

Figure 16. Fitted curves of BS4–BS6.

Using x_{50} as the indicator for evaluating the effect of blast fragmentation in this study, Figure 17 shows the histograms of median size versus delay time. As shown in Figure 17, BS6 obtained the best fragmentation, while BS3 achieved the worst fragmentation. In addition, Figure 7 shows that in the range of 0–100 μs, the increase in delay time did not effectively improve fragmentation, shown by BS3 obtaining the maximum x_{50} value. In the inter-hole delay of 100–250 μs, x_{50} gradually decreased as delay time increased. When the inter-hole delay reached 250 μs, the median size of BS6 decreased by approximately 48.7% compared to that of BS3, which means that fragmentation was significantly improved.

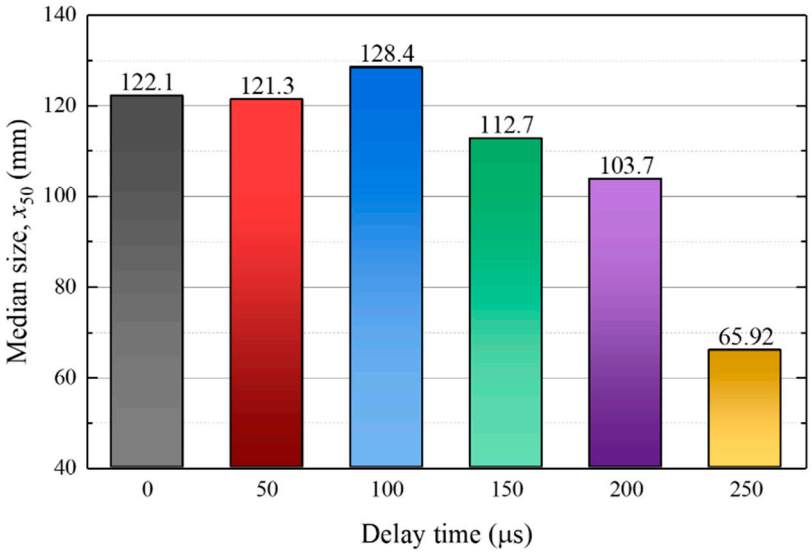

Figure 17. Median size of each bench specimen.

Figure 18 shows the connected scatterplots of the median sizes and blast excavation weights of all specimens. The black line of the connected scatterplots represents the variation in median size, the red line of the connected scatterplots represents the variation

in blast excavation weight, and the blue dashed square represents the location of the best blast excavation quality. As shown in Figure 18, although BS6 produced the smallest median size, it also obtained the minimum blast excavation weight of 47.2 kg. BS3, with the maximum blast excavation weight of 85.2 kg, produced the largest median size, and the particle size in the coarse zone was significantly larger than that of the other experiments. In the remaining four blasting experiments, BS5 obtained the smallest median size and the maximum blast excavation weight of 65.9 kg. Considering the blast excavation weights and the obtained fragmentation distribution results of all bench specimens, BS5 recorded the best blast excavation quality, with the optimum delay time being 200 μs.

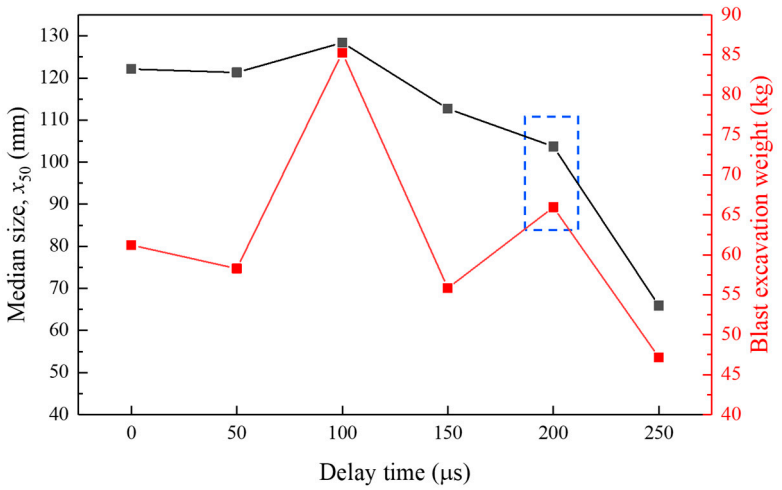

Figure 18. Median sizes and blast excavation weights of all specimens with different delays.

4. Discussion

This experimental study of the effect of delay time on rock fragmentation shows there is a certain delay requirement related to obtaining optimal blast excavation quality in multi-hole bench blasting. The location of stress waves between boreholes plays an important role in wave history and possibly influences rock damage and fragmentation. Therefore, a brief analysis of the stress waves produced by the boreholes was performed in the 2D horizontal plane. Figure 19 shows the P-wave propagation produced by the borehole at three delays. The solid line represents the P-wave, and the dashed line represents the reflected P-wave.

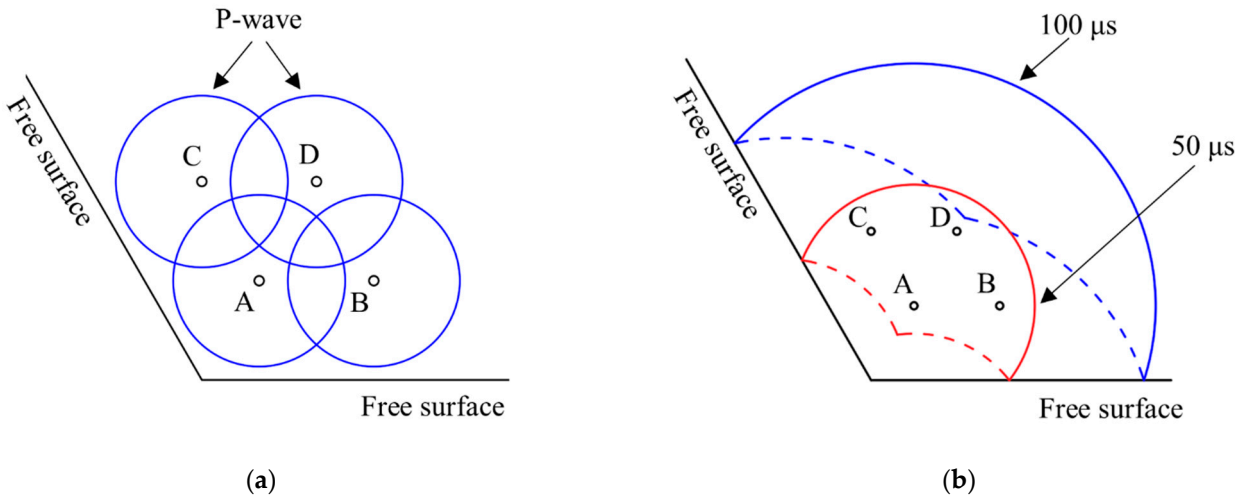

Figure 19. Brief analysis of P-wave propagation: (**a**) P-wave propagation for simultaneous detonation; (**b**) P-wave propagation of borehole A at 50 μs and 100 μs. The letters A–D represent the numbers of the boreholes.

After the explosive column is detonated in the borehole, the stress wave propagates within the bench specimen. Figure 19a shows the P-wave propagation of simultaneous detonations, with the most significant superposition of P-waves occurring in the area between boreholes. The location of the P-wave superposition changes when there is a delay between the boreholes. P-wave propagation at 50 μs after the detonation of borehole A is shown in Figure 19b. If the inter-hole delay is 50 μs, the reflected P-wave of borehole A formed at the free surface will interact with the P-wave generated by borehole B in the burden. When the inter-hole delay is 100 μs, the P-wave propagation of borehole A when borehole B is detonated is as shown in Figure 19b. At this time, the reflected wave of borehole A formed at the free surface propagates to the back of borehole B, indicating that there is no P-wave superposition in the burden. The same P-wave analysis method can be applied to bench specimens BS4–BS6. When the inter-hole delay increases, the interaction of the P-waves in the burden becomes weaker until it disappears.

BS1, with the most significant stress wave superposition in the blasting experiments, did not produce the smallest median size. When the inter-hole delay was increased to 50 μs, BS2 produced an x_{50} value similar to that of BS1. In the coarse zone, the particle size of BS2 was decreased compared to BS1, which means rock fragmentation was improved in this zone. Unfortunately, the further increase in delay time did not continue to improve fragmentation, and BS3 obtained the worst fragmentation results. Although BS3 recorded the maximum blast excavation weight, the particle size in the coarse zone of BS3 was also significantly increased, with the x_{max} value increasing by nearly 21.3% compared to that of BS1. In the blasting experiments of BS4–BS6, the interaction of the stress waves gradually became weaker until it disappeared, and the particle size in 1–80% mass passing decreased with the increased inter-hole delay. BS6, having the longest delay time of all experiments, obtained the smallest x_{50} value, i.e., the best fragmentation result. Compared to BS1 with simultaneous detonation, the x_{50} value of BS6 was improved by nearly 46%. In this study, simultaneous detonation and short delays did not obtain excellent fragmentation results. When the inter-hole delay was longer than 100 μs, fragmentation was improved with increased delay time, even though stress wave interaction gradually disappeared. This indicates that other factors besides stress wave interaction should be considered in multi-hole delay blasting to control fragmentation.

In studying stress wave propagation in rock using different delay times, the rock medium is usually treated as an intact continuum, and the propagation of cracks in the rock mass is often ignored. During blasting, the velocity of the blast-induced crack is lower than that of the stress wave. By conducting model blast tests, Bergmann et al. [52] found that the crack velocity of granite is about one-third of its P-wave velocity. In short delays, the cracks around the borehole do not have enough time to grow. When the delay time between boreholes increases, the propagation time of the cracks produced by the first borehole that is detonated also increases. According to the longitudinal wave velocity of the granite in this paper, the blast-induced crack velocity in the bench specimen is approximately 1128 m/s. As the inter-hole delay increases, the crack around the first borehole that is detonated propagates outward. For example, at 150 μs, the blast-induced crack propagation distance reaches approximately 169 mm. The rock around the borehole at this time is already a discontinuous medium, which affects the propagation of stress waves generated by subsequent boreholes. For the subsequent boreholes, the blast-induced cracks from adjacent boreholes provide more complex boundary conditions for blasting. For long delay times, the blast-induced crack propagation time should be considered as an influential factor when choosing the optimal delay time in bench blasting, which may be beneficial for better understanding of the effect of delays on rock fragmentation.

5. Conclusions

Six blasting experiments were conducted using bench specimens with four boreholes. The following conclusions can be made:

1. Delay time markedly influenced full-field strain on the monitored front surface of the bench specimen. The strain field results analyzed using the 3D-DIC technique show that the surface strain field transformed from horizontal strain concentration zone dominated to vertical strain concentration zone dominated as the delays increased.
2. It was observed that short delays with a stress wave superposition produced a larger range of toe rock above the bench floor compared to long delays. The maximum blast excavation weight of 85.2 kg was obtained for BS3 with an inter-hole delay of 100 μs, while the smallest blast excavation weight of 47.1 kg was obtained for BS6 with the longest inter-hole delay.
3. The fragment size distributions were well constructed by the extended Swebrec function. The fragmentation results indicate that stress wave superposition had a limited effect on improving rock fragmentation. For long delay times without stress wave interaction, rock fragmentation improved as delay time increased. BS6, with the longest delay time, obtained the best fragment size distribution.
4. By combining blast excavation weights and the fragment size distribution of all experiments, BS5 produced the best blast excavation quality, and the optimum delay time was 200 μs.
5. This study investigated the effect of delay time on rock fragmentation through model blasting. In the future, full-scale benches should be used to conduct similar experiments. Furthermore, the influence of crack propagation on fragmentation can be further investigated by combining numerical simulations, which is instrumental for understanding the effect of the mechanism of delay time on rock fragmentation.

Author Contributions: Conceptualization, J.Y. and Q.Y.; methodology, H.-L.T. and Q.Y.; software, Q.Y.; validation, J.Y.; formal analysis, H.-L.T.; investigation, H.-L.T.; resources, J.Y.; data curation, H.-L.T. and Q.Y.; writing—original draft preparation, H.-L.T.; writing—review and editing, H.-L.T. and J.Y.; visualization, H.-L.T. and Q.Y.; supervision, J.Y. and Q.Y.; project administration, J.Y.; funding acquisition, J.Y. All authors have read and agreed to the published version of the manuscript.

Funding: This research was funded by the National Natural Science Foundation of China, grant numbers 51774043.

Institutional Review Board Statement: Not applicable.

Informed Consent Statement: Not applicable.

Data Availability Statement: Not applicable.

Conflicts of Interest: The authors declare no conflict of interest.

References

1. Bayat, P.; Monjezi, M.; Rezakhah, M.; Armaghani, D.J. Artificial Neural Network and Firefly Algorithm for Estimation and Minimization of Ground Vibration Induced by Blasting in a Mine. *Nat. Resour. Res.* **2020**, *29*, 4121–4132. [CrossRef]
2. Faradonbeh, R.S.; Hasanipanah, M.; Amnieh, H.B.; Armaghani, D.J.; Monjezi, M. Development of GP and GEP models to estimate an environmental issue induced by blasting operation. *Environ. Monit. Assess.* **2018**, *190*, 351. [CrossRef] [PubMed]
3. Persson, P.-A.; Holmberg, R.; Lee, J. *Rock Blasting and Explosives Engineering*; CRC Press: Boca Raton, FL, USA, 1993; ISBN 084938978X.
4. Zhang, Z.-X.; Chi, L.Y.; Qiao, Y.; Hou, D.-F. Fracture Initiation, Gas Ejection, and Strain Waves Measured on Specimen Surfaces in Model Rock Blasting. *Rock Mech. Rock Eng.* **2021**, *54*, 647–663. [CrossRef]
5. Chi, L.Y.; Zhang, Z.-X.; Aalberg, A.; Yang, J.; Li, C.C. Measurement of shock pressure and shock-wave attenuation near a blast hole in rock. *Int. J. Impact Eng.* **2019**, *125*, 27–38. [CrossRef]
6. Zhang, Z.-X. *Rock Fracture and Blasting: Theory and Applications*; Butterworth-Heinemann: Oxford, UK, 2016; ISBN 0128027045.
7. Armaghani, D.J.; Hajihassani, M.; Mohamad, E.T.; Marto, A.; Noorani, S.A. Blasting-induced flyrock and ground vibration prediction through an expert artificial neural network based on particle swarm optimization. *Arab. J. Geosci.* **2014**, *7*, 5383–5396. [CrossRef]
8. Ghoraba, S.; Monjezi, M.; Talebi, N.; Moghaddam, M.R.; Armaghani, D.J. Prediction of ground vibration caused by blasting operations through a neural network approach: A case study of Gol-E-Gohar Iron Mine, Iran. *J. Zhejiang Univ. Sci. A Appl. Phys. Eng.* **2015**, *119*, 1631.

9. Hajihassani, M.; Jahed Armaghani, D.; Marto, A.; Tonnizam Mohamad, E. Ground vibration prediction in quarry blasting through an artificial neural network optimized by imperialist competitive algorithm. *Bull. Eng. Geol. Environ.* **2015**, *74*, 873–886. [CrossRef]
10. Hino, K. Theory of blasting with concentrated charge. *J. Ind. Explos. Soc. Japan* **1954**, *15*, 233–249.
11. Duvall, W.I.; Atchison, T.C. *Rock Breakage by Explosives*; US Bureau of Mines: Pittsburgh, PA, USA, 1957; Volume 5356.
12. Langefors, U.; Kihlström, B. *The Modern Technique of Rock Blasting*; Wiley: New York, NY, USA, 1963; Volume 405.
13. Clark, L.D.; Saluja, S.S. Blasting mechanics. *Trans. Am. Inst. Min. Metall. Eng.* **1964**, *229*, 78–90.
14. Kutter, H.K.; Fairhurst, C. On the fracture process in blasting. *Int. J. Rock Mech. Min. Sci. Geomech. Abstr.* **1971**, *8*, 181–202. [CrossRef]
15. Field, J.E.; Ladegaard-Pedersen, A. The importance of the reflected stress wave in rock blasting. *Int. J. Rock Mech. Min. Sci. Geomech. Abstr.* **1971**, *8*, 213–226. [CrossRef]
16. Fourney, W.L.; Holloway, D.C.; Dally, J.W. Fracture initiation and propagation from a center of dilatation. *Int. J. Fract.* **1975**, *11*, 1011–1029. [CrossRef]
17. Fourney, W.L. The role of stress waves and fracture mechanics in fragmentation. *Blasting Fragm.* **2015**, *9*, 83–106.
18. Johansson, C.H.; Persson, P.-A. *Detonics of High Explosives*; Academic Press: Cambridge, MA, USA, 1970.
19. Xahykaeb, A.H. *Physical Process of Rock Blasting in Mining*; Mineral Press: Leningrad, Russia, 1974.
20. Hashemi, A.S.; Katsabanis, P. The effect of stress wave interaction and delay timing on blast-induced rock damage and fragmentation. *Rock Mech. Rock Eng.* **2020**, *53*, 2327–2346. [CrossRef]
21. Holloway, D.C. Application of holographic interferometry to stress wave and crack propagation problems. *Opt. Eng.* **1982**, *21*, 468–473. [CrossRef]
22. Ledoux, L. The Role of Stress Waves and Gases in the Development of Fragmentation. Master's Thesis, Queen's University, Kingston, ON, Canada, 2016.
23. Rossmanith, H.P. The Use of Lagrange Diagrams in Precise Initiation Blasting. Part I: Two Interacting Blastholes. *Fragblast* **2002**, *6*, 104–136. [CrossRef]
24. Rossmanith, H.P.; Kouzniak, N. Supersonic Detonation in Rock Mass-Part 2: Particle Displacements and Velocity Fields for Single and Multiple Non-Delayed and Delayed Detonating Blastholes. *Fragblast* **2004**, *8*, 95–117. [CrossRef]
25. Vanbrabant, F.; Espinosa, A. Impact of short delays sequence on fragmentation by means of electronic detonators: Theoretical concepts and field validation. *Fragblast* **2006**, *8*, 326–331.
26. Chiappetta, F. Combining electronic detonators with stem charges and air decks. In Proceedings of the Drill and Blast 2010 Conference, Brisbane, Australia, 28–29 April 2010.
27. Johansson, D.; Ouchterlony, F. Shock Wave Interactions in Rock Blasting: The Use of Short Delays to Improve Fragmentation in Model-Scale. *Rock Mech. Rock Eng.* **2013**, *46*, 1–18. [CrossRef]
28. Katsabanis, P.D.; Tawadrous, A.; Braun, C.; Kennedy, C. Timing effects on the fragmentation of small scale blocks of granodiorite. *Fragblast* **2006**, *10*, 83–93. [CrossRef]
29. Stagg, M.S.; Rholl, S.A. Effects of accurate delays on fragmentation for single-row blasting in a 6.7 m (22 ft) bench. *Fragblast* **1987**, *2*, 210–230.
30. Tang, H.-L.; Liu, X.; Yang, J.; Yu, Q. Experimental Study on the Influence of Delay Time on Rock Fragmentation in Bench Blasting. *Appl. Sci.* **2023**, *13*, 85. [CrossRef]
31. Schill, M.; Sjöberg, J. Finite Element simulations of blasting and fragmentation with precise initiation. In Proceedings of the 12th International LS-DYNA Users Conference, Detroit, MI, USA, 3–5 June 2012; pp. 1–10.
32. Yi, C.; Johansson, D.; Nyberg, U.; Beyglou, A. Stress wave interaction between two adjacent blast holes. *Rock Mech. Rock Eng.* **2016**, *49*, 1803–1812. [CrossRef]
33. Yi, C.; Sjöberg, J.; Johansson, D.; Petropoulos, N. A numerical study of the impact of short delays on rock fragmentation. *Int. J. Rock Mech. Min. Sci.* **2017**, *100*, 250–254. [CrossRef]
34. Blair, D.P. Limitations of electronic delays for the control of blast vibration and fragmentation. In Proceedings of the 9th International Symposium on Rock Fragmentation by Blasting, Granada, Spain, 13–17 August 2009; p. 171.
35. Zhang, Z.-X.; Hou, D.-F.; Guo, Z.; He, Z.; Zhang, Q. Experimental study of surface constraint effect on rock fragmentation by blasting. *Int. J. Rock Mech. Min. Sci.* **2020**, *128*, 104278. [CrossRef]
36. Chi, L.Y.; Zhang, Z.-X.; Aalberg, A.; Li, C.C. Experimental Investigation of Blast-Induced Fractures in Rock Cylinders. *Rock Mech. Rock Eng.* **2019**, *52*, 2569–2584. [CrossRef]
37. Cho, S.H.; Nishi, M.; Yamamoto, M.; Kaneko, K. Fragment size distribution in blasting. *Mater. Trans.* **2003**, *44*, 951–956. [CrossRef]
38. Sanchidrian, J.A.; Segarra, P.; Ouchterlony, F.; Gomez, S. The influential role of powder factor vs. delay in full-scale blasting: A perspective through the fragment size-energy fan. *Rock Mech. Rock Eng.* **2022**, *55*, 4209–4236. [CrossRef]
39. Spranghers, K.; Vasilakos, I.; Lecompte, D.; Sol, H.; Vantomme, J. Full-field deformation measurements of aluminum plates under free air blast loading. *Exp. Mech.* **2012**, *52*, 1371–1384. [CrossRef]
40. Lenoir, N.; Bornert, M.; Desrues, J.; Bésuelle, P.; Viggiani, G. Volumetric digital image correlation applied to X-ray microtomography images from triaxial compression tests on argillaceous rock. *Strain* **2007**, *43*, 193–205. [CrossRef]
41. Bornert, M.; Vales, F.; Gharbi, H.; Nguyen Minh, D. Multiscale full-field strain measurements for micromechanical investigations of the hydromechanical behaviour of clayey rocks. *Strain* **2010**, *46*, 33–46. [CrossRef]

42. Hedan, S.; Cosenza, P.; Valle, V.; Dudoignon, P.; Fauchille, A.-L.; Cabrera, J. Investigation of the damage induced by desiccation and heating of Tournemire argillite using digital image correlation. *Int. J. Rock Mech. Min. Sci.* **2012**, *51*, 64–75. [CrossRef]
43. Cheng, J.-L.; Yang, S.-Q.; Chen, K.; Ma, D.; Li, F.-Y.; Wang, L.-M. Uniaxial experimental study of the acoustic emission and deformation behavior of composite rock based on 3D digital image correlation (DIC). *Acta Mech. Sin.* **2017**, *33*, 999–1021. [CrossRef]
44. Xing, H.Z.; Zhang, Q.B.; Ruan, D.; Dehkhoda, S.; Lu, G.X.; Zhao, J. Full-field measurement and fracture characterisations of rocks under dynamic loads using high-speed three-dimensional digital image correlation. *Int. J. Impact Eng.* **2018**, *113*, 61–72. [CrossRef]
45. Xu, X.; Chi, L.-Y.; Yang, J.; Yu, Q. Experimental Study on the Temporal and Morphological Characteristics of Dynamic Tensile Fractures in Igneous Rocks. *Appl. Sci.* **2021**, *11*, 11230. [CrossRef]
46. Xu, X.; Chi, L.-Y.; Yang, J.; Lv, N. Investigation on the Deformation and Failure Characteristics of Concrete in Dynamic Splitting Tests. *Materials* **2022**, *15*, 1681. [CrossRef]
47. Chi, L.Y.; Zhang, Z.X.; Aalberg, A.; Yang, J.; Li, C.C. Fracture Processes in Granite Blocks Under Blast Loading. *Rock Mech. Rock Eng.* **2019**, *52*, 853–868. [CrossRef]
48. Ouchterlony, F. The Swebrec function: Linking fragmentation by blasting and crushing. *Min. Technol.* **2005**, *114*, 29–44. [CrossRef]
49. Ouchterlony, F. *Fragmentation Characterization: The Swebrec Function and Its Use in Blast Engineering Rock Fragmentation by Blasting*; Sanchidrián, J.A., Ed.; Taylor & Francis Group: London, UK, 2010.
50. Sanchidrián, J.A.; Ouchterlony, F.; Moser, P. Performance of some distributions to describe rock fragmentation data. *Int. J. Rock Mech. Min. Sci.* **2012**, *53*, 18–31. [CrossRef]
51. Sanchidrián, J.A.; Ouchterlony, F.; Segarra, P.; Moser, P. Size distribution functions for rock fragments. *Int. J. Rock Mech. Min. Sci.* **2014**, *71*, 381–394. [CrossRef]
52. Bergmann, O.R.; Riggle, J.W.; Wu, F.C. Model rock blasting—Effect of explosives properties and other variables on blasting results. *Int. J. Rock Mech. Min. Sci. Geomech. Abstr.* **1973**, *10*, 585–612. [CrossRef]

Disclaimer/Publisher's Note: The statements, opinions and data contained in all publications are solely those of the individual author(s) and contributor(s) and not of MDPI and/or the editor(s). MDPI and/or the editor(s) disclaim responsibility for any injury to people or property resulting from any ideas, methods, instructions or products referred to in the content.